Multiresolution analysis of inertial particle tessellations for clustering dynamics

By K. Matsuda†, K. Schneider‡, T. Oujia‡, J. West, S. S. Jain AND K. Maeda

We propose a multiresolution tessellation technique to analyze multiscale statistics of particle velocity divergence defined at discrete particle positions. Our approach enables computation of the scale-dependent divergence by leveraging a wavelet transformation of Lagrangian point particle data and is important for characterizing particle clustering in turbulent flows. The technique is systematically verified by using synthetic data of randomly distributed particles in a two-dimensional plane. We demonstrate the technique by extracting the scale-dependent particle velocity divergence of inertial particles in homogeneous isotropic turbulence from direct numerical simulation data. The result is verified by comparing the energy spectrum of the divergence with that obtained by a Fourier-based approach.

1. Introduction

Inertial heavy particles suspended in high–Reynolds number turbulence are ubiquitous in geophysical and industrial flows; e.g., cloud droplets in atmospheric flows, dust particles in protoplanetary disks, and spray combustion. The inertial particles form nonuniform spatial distribution (i.e., clustering) in turbulence, because the particles are swept out from turbulent eddies and concentrate in low vorticity and high–strain rate regions. The particle clustering in high–Reynolds number turbulence has multiscale structures. Recently, Matsuda *et al.* (2021) showed the cluster/void pronounced structures of inertial particle clustering depend on the spatial scale and the Stokes number. Therefore, to predict the particle behavior, it is important to understand and model the multiscale dynamics of the particle clustering. The key quantity to evaluate the particle cluster formation is the divergence of the particle velocity. However, it is still challenging to obtain multiscale particle velocity divergence information based on discrete Lagrangian particle position and velocity data, i.e., particle cloud data.

Tools from discrete mathematics enable efficient description and representation of particle cloud data, for instance tessellations and graphs, which have been successfully used in various applications, for example in neuroscience and telecommunication. Oujia *et al.* (2020) proposed a tessellation technique to calculate the particle velocity divergence using the position and velocity of Lagrangian particles. This technique allows us to access the particle velocity divergence at a particle position based on the temporal rate of change in volume of a tessellation cell. The use of a graph representation of the particle data, i.e., a mathematical structure of vertices and edges, then permits the application of signal-processing techniques on graphs, a growing subject over the last years—see, e.g., Shuman *et al.* (2013). In particular, multiresolution analysis, which is related to wavelets, can be constructed and applied to tessellations. Thus, tessellations can be coarse-grained and refined to obtain scale information. Multiresolution constructions were originally developed

† Japan Agency for Marine-Earth Science and Technology (JAMSTEC), Japan
‡ Institut de Mathématiques de Marseille, Aix-Marseille Universit, CNRS, France

on Cartesian grids (Mallat 1999), and generalizations for triangles can be found in Cohen *et al.* (2000) and Yu & Ra (1999). Wavelets on graphs have been likewise constructed in Avena *et al.* (2020). In the current paper, we develop a straightforward approach to construct a multiresolution analysis on graphs having the multiscale decomposition of the particle velocity divergence in mind. Coarsening and refinement operators are introduced and wavelet coefficients are defined as details between two levels. A fast algorithm for this purpose is proposed that works efficiently for millions of particles, and thus scale decomposition of the particle velocity divergence can be determined, yielding insight into the multiscale dynamics of clustering.

This report is organized as follows. In Section 2, the basic equations for the concerned particle-laden flows and the tessellation technique to analyze the particle velocity divergence are briefly outlined. The proposed multiresolution technique is described in Section 3. Sections 4 and 5 present the results from application of the proposed technique to two-dimensional (2D) data of random particles with artificial signals and three-dimensional (3D) data of inertial particles with the particle velocity divergence data in homogeneous isotropic turbulence (HIT), respectively. Finally, conclusions are summarized in Section 6.

2. Particle-laden flows and particle velocity divergence

We consider the Navier–Stokes and continuity equations for an incompressible flow,

$$\frac{\partial \boldsymbol{u}}{\partial t} + (\boldsymbol{u}\cdot\nabla)\boldsymbol{u} = -\frac{1}{\rho}\nabla p + \nu\nabla^2\boldsymbol{u} + \boldsymbol{f}\ , \qquad \nabla\cdot\boldsymbol{u} = 0, \tag{2.1}$$

where $\boldsymbol{u}(\boldsymbol{x})$ is the fluid velocity field, $p(\boldsymbol{x})$ is the pressure, ρ is the fluid density, ν is the kinematic viscosity, and $\boldsymbol{f}(\boldsymbol{x})$ is an external forcing. The Lagrangian motion of small and heavy inertial particles in a fluid flow can be modeled by the following equations based on the point particle assumption,

$$\frac{d\boldsymbol{x}_p}{dt} = \boldsymbol{v}_p\ , \qquad \frac{d\boldsymbol{v}_p}{dt} = -\frac{\boldsymbol{v}_p - \boldsymbol{u}(\boldsymbol{x}_p)}{\tau_p}, \tag{2.2}$$

where $\boldsymbol{x}_p$ is the particle position, $\boldsymbol{v}_p$ is the particle velocity, and τ_p is the particle relaxation time. The term on the right-hand side of the second equation in Eq. (2.2) is the drag force term. Here, we assume that the particle density is sufficiently larger than the fluid density and that the effect of gravitational settling is negligibly small. When the particles are moving in a turbulent flow, statistics of the particle clustering depend on the Stokes number St, defined as the ratio of τ_p and a flow time scale.

The particle-clustering mechanism can be discussed based on the conservation equation of the particle number density field $n(\boldsymbol{x})$ in continuous setting. If there is no external source or sink for the particle number density, the conservation equation is given by

$$\frac{\partial n}{\partial t} + \boldsymbol{v}\cdot\nabla n = -n\nabla\cdot\boldsymbol{v}, \tag{2.3}$$

where $\boldsymbol{v}(\boldsymbol{x})$ is the particle velocity field in continuous setting. This means that the source and sink for the number density n along the Lagrangian particle trajectory are given by the term on the right-hand side, and the negative/positive values of the particle velocity divergence $\nabla\cdot\boldsymbol{v}$ contribute to the cluster formation/destruction, respectively. If the particles are tracers, which perfectly follow the fluid motion, the particle velocity divergence $\nabla\cdot\boldsymbol{v}$ becomes zero in an incompressible flow and the particle clustering does

not occur. Thus, the source of clustering is the deviation of particle motion from the fluid flow. Maxey (1987) evaluated the particle velocity divergence using an approximation for $St \ll 1$. Maxey's approximation yields that $\nabla \cdot \boldsymbol{v}$ is proportional to the second invariant of the velocity gradient tensor, and it explains the preferential concentration mechanism. However, the approximation is not valid for particles with $St \gtrsim 1$, which show significant particle clustering.

The particle distribution and velocity data can be obtained by performing direct numerical simulation (DNS) of particle-laden flows in which the fluid flow field $\boldsymbol{u}(\boldsymbol{x})$ is obtained by solving Eq. (2.1) on Eulerian grid points, and the particle position and velocity are obtained by solving Eq. (2.2) based on the Lagrangian method. The difficulty of calculating the particle velocity divergence is due to the discrete nature of particles. To compute the particle velocity divergence based on the DNS data, Oujia *et al.* (2020) proposed a tessellation technique based on the temporal rate of change in volumes. The particle velocity divergence $\mathcal{D}(\boldsymbol{x}_p) = (\nabla \cdot \boldsymbol{v})(\boldsymbol{x}_p)$ at the particle position $\boldsymbol{x}_p$ is given by $\mathcal{D}(\boldsymbol{x}_p) = (1/V)(DV/Dt)$, where V is the volume of the tessellation cell that contains the particle at $\boldsymbol{x}_p$. To define the tessellation cells around a particle, Oujia *et al.* (2020) used the Voronoï tessellation, and recently Oujia *et al.* (2022) used the center of gravity of the Delaunay tetrahedron for the vertex of the cell for a stability reason. The tessellation technique allows us to access the particle divergence values at the particle positions. However, to analyze the multiscale clustering dynamics, it is necessary to develop a multiresolution tessellation technique for the particle velocity divergence data.

3. Construction of multiresolution analysis on graphs

3.1. *A primer on multiresolution analysis on regular grids*

We consider a discrete signal $\{s_n\} = \{\bar{s}_{J,n}\} \in \mathbb{R}^N$on one-dimensional (1D) equidistant grids at $\{x_{J,n}\} \in \mathbb{R}^N$, where $N = 2^J$ and the scale of the grid spacing is 2^{-J}. Note that the signal can be a spatial field data sampled at discrete points distributed in the space. For the multiresolution analysis, the signal on 2^J grid points is projected to 2^{J-1} grid points at $x_{J-1,i} = x_{J,2i}$ for $i = 0, \cdots, 2^{J-1} - 1$. Hence, the scale of grid spacing becomes $2^{-(J-1)}$. The coarsening of the signal can be described by

$$\bar{s}_{J-1,i} = P_{J \to J-1}\{\bar{s}_{J,n}\}, \tag{3.1}$$

where $\bar{s}_{J-1,i}$ is the signal at $x_{J-1,i}$ at the coarser scale, and $P_{J \to J-1}$ is the projection operator. By applying the projection operator to the coarser signal recursively, we can define the signal $\{\bar{s}_{j,n}\}$ at the scale 2^{-j} $(j = 0, \cdots, J-1)$, where the scale index j decreases as the scale becomes coarser. Figure 1 shows the relationship between the scale 2^{-j} and $2^{-(j-1)}$. The signal $\{\bar{s}_{j,n}\}$ at the scale 2^{-j} can be projected to the scale $2^{-(j-1)}$ based on Eq. (3.1), with J replaced by j. The signal at the finer scale 2^{-j} can be predicted by using the signal at the scale $2^{-(j-1)}$,

$$\hat{s}_{j,2i+1} = P_{j-1 \to j}\{\bar{s}_{j-1,n}\}, \tag{3.2}$$

where $\hat{s}_{j,i}$ is the predicted signal at $x_{j,i}$, and $P_{j-1 \to j}$ is the prediction operator. The detail information confined in space and scale can be then defined as the difference between the original and the predicted signal,

$$d_{j-1,i} = \bar{s}_{j,2i+1} - \hat{s}_{j,2i+1}, \tag{3.3}$$

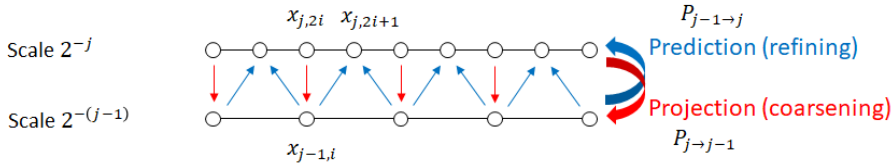

FIGURE 1. Illustration of projection and prediction operators for 1D regular grids.

where $d_{j,i}$ is the detail coefficient for the scale index j and the position index i. The projection and prediction operators determine the characteristics of the multiresolution analysis. For the wavelet transform, the operators must satisfy

$$P_{j\to j-1} \circ P_{j-1\to j} = Id, \tag{3.4}$$

where $\circ$ is the composition operator and Id the identity.

3.2. *Multiresolution graphs*

To construct a multiresolution technique for a signal on discrete particle positions, it is necessary to define the projection and prediction operators, and these operators require the information of neighbor particles. Since we use the tessellation to obtain the particle velocity divergence data, the neighbor particles can be specified as the particles in the neighbor tessellation cells. The cell for each particle and the neighbor cells are connected by the edges obtained from Delaunay tessellation. Therefore, the particles and the edges of Delaunay tessellation can be considered to be an undirected graph that represents the neighbor cells.

In mathematics, a graph is defined as vertices connected by edges. To apply multiresolution analysis on graphs, multiresolution graphs are needed. Here, the multiresolution graph construction starts from the finest scale, which is level 0. Therefore, we use the level index $l = 0, \cdots, L-1$, which increases as the scale becomes larger. Note that the constructed graphs do not change even when increasing the number of levels L. The coarser graph at level $l+1$ is constructed from the finer graph at level l. For the graph coarsening, we adopted the half-edge collapse operator (Kobbelt *et al.* 1998), in which one vertex is merged with an adjacent vertex. Figure 2 shows the schematic diagram of the merging process. Here, the vertex P_1 is merged to the vertex P_2, and P_1 is removed. The edges connected to P_1 and P_2 are integrated. Based on the analogy to the 1D regular grid case, P_1 and P_2 can be considered to be the odd and even vertices. Since we consider particle distributions in the physical space, we assume that each particle (i.e., each vertex on the graph) has the information of the tessellation cell volume. The algorithm for constructing the graph at level $l+1$ from the graph at level l is as follows: (i) Select the vertex with the minimum volume among all the unmarked vertices on the graph, and consider it to be the odd vertex. (ii) Select the vertex with the minimum volume among the unmarked vertices neighboring to the odd vertex, and consider it to be the even vertex. (iii) Merge the odd vertex to the even vertex: The odd vertex is removed, and the even vertex is marked to be shifted to level $l+1$. If there is no unmarked neighbor vertex at step (ii), the odd vertex is marked and shifted to level $l+1$ without the merging process. Steps (i)–(iii) are repeated until all the vertices are marked.

The volume conservation is a key feature to represent the physics on the graph. Therefore, the volume value of the marked vertex is updated to the sum of the volumes attributed to the even and odd vertices. When the volume attributed to the even and odd vertices at level l are given by V_{2i}^l and V_{2i+1}^l, respectively, the volume attributed to the

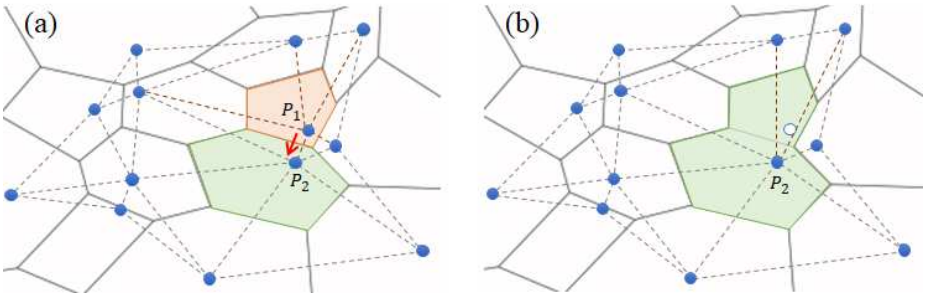

FIGURE 2. The point-merging process on the Delaunay graph. (a) The graph before merging. The edges of the Delaunay graph represent the neighboring cells. The odd point P_1 will be merged to the even point P_2. (b) The graph after merging. The graph edges are modified to represent connection with the cells neighboring the merged cell.

vertex marked and shifted to level $l+1$ satisfies $V_i^{l+1} = V_{2i}^l + V_{2i+1}^l$. If the odd vertex is shifted to level $l+1$ without the merging process, the volume value is not updated.

3.3. *Wavelet transform on graphs*

Here, we consider a signal $s_i^0 = s^0(\boldsymbol{x}_{p,i})$ $(i = 0, \cdots, N_p - 1)$ on discrete particle positions (i.e., vertices on a graph). Since we aim to apply the multiresolution analysis to the particle velocity divergence data, we propose the wavelet transform on graphs based on the following conservation equation

$$V_i^{l+1}\bar{s}_i^{l+1} = V_{2i}^l \bar{s}_{2i}^l + V_{2i+1}^l \bar{s}_{2i+1}^l, \tag{3.5}$$

where $\bar{s}_i^l$ is the signal of the ith vertex on the graph at level l, and the index $2i$ and $2i+1$ represents the even and odd vertices, respectively. The projection operator is then defined as

$$\bar{s}_i^{l+1} = \frac{1}{V_i^{l+1}}(V_{2i}^l \bar{s}_{2i}^l + V_{2i+1}^l \bar{s}_{2i+1}^l). \tag{3.6}$$

For the prediction operator, we simply assume that the predicted values are the same as the projected signals at the coarser level,

$$\hat{s}_{2i}^l = \bar{s}_i^{l+1}, \ \hat{s}_{2i+1}^l = \bar{s}_i^{l+1}. \tag{3.7}$$

The prediction and projection operators satisfy the identity (3.4). The detail coefficient (i.e., the wavelet coefficient) is then given by the difference between the original and predicted signals, yielding

$$d_i^{l+1} = \frac{V_{2i}^l}{V_i^{l+1}}(\bar{s}_{2i+1}^l - \bar{s}_{2i}^l). \tag{3.8}$$

The wavelet coefficient based on the L^2 normalization can be obtained by multiplying the detail coefficients with the scaling factor $\sigma_i^{l+1} = \sqrt{V_i^{l+1} V_{2i+1}^l / V_{2i}^l}$.

For multiscale statistics of the signal on discrete particle positions, we can consider q^{th} order moments of details d_i^l,

$$M_q[d_i^l] = \frac{1}{N^l}\sum_{i=1}^{N^l}(d_i^l)^q, \tag{3.9}$$

where N^l is the number of detail coefficients at level l.

4. Application to 2D test cases

The multiresolution tessellation is applied to random particle distributions in a 2D square domain with edge length 2π. Two types of signals are generated for the signal value of each particle instead of the particle velocity divergence data. The first one is a Gaussian noise of $\mathcal{N}(0,1)$, i.e., zero mean and unit variance. The second one is a spectral signal defined as

$$s_i^0 = s^0(\boldsymbol{x}_{p,i}) = A^{-1} \sum_{k_x=1}^{N_k} \sum_{k_y=1}^{N_k} a(|\boldsymbol{k}|) \sin[k_x x_{p,i} + \theta_x(\boldsymbol{k})] \sin[k_y y_{p,i} + \theta_y(\boldsymbol{k})], \tag{4.1}$$

where $\boldsymbol{x}_{p,i} = (x_{p,i}, y_{p,i})$, $\boldsymbol{k} = (k_x, k_y)$, $a(|\boldsymbol{k}|) = \exp[-|\boldsymbol{k}|^2\pi^2/(24k_c^2)]$ is the Gaussian filtered amplitude for the cutoff wave number of $k_c = 20$, and $\theta_x(\boldsymbol{k}) \in [0, 2\pi)$ and $\theta_y(\boldsymbol{k}) \in [0, 2\pi)$ are the random phase shifts. The signal is normalized by A so that the standard deviation of s_i^0 becomes unity. This signal is also a Gaussian noise but is spatially correlated due to the low-pass filtered amplitude. The Fourier energy spectrum of the signal is proportional to $k|a(k)|^2$, where $k = |\boldsymbol{k}|$. Thus, the spectrum is approximately proportional to k^1 for $k \ll k_c$ and has a peak at $k \approx 0.78\ k_c$.

The tessellation cells and the projected signals $\bar{s}_i^l$ for each level l for the Gaussian noise are visualized in Figure 3. The number of particles is $N_p = 10^4$. The signals are normalized by the standard deviation of the signal at each level. We can observe that the size of the same color regions increases as the level increases, and this indicates that the tessellations at different levels have different spatial scales.

Figure 4 shows the statistics obtained from the 2D multiresolution analyses for $N_p = 10^5$. Figure 4(a) presents the probability density function (PDF) of volume V_i^l for each level l. The volume is normalized by the mean volume $V_{\mathrm{mean}} = (2\pi)^D/N_p$, where D is the space dimension. As the level increases, the peak of the PDF shifts to larger volumes. Here, we also use the volume information for defining the spatial scale: The volume scale d_V is defined as $d_V = [(1/N^l)\sum_{i=1}^{N^l} V_i^l]^{1/D}$. Note that the obtained d_V is approximately proportional to $2^{l/D}$. The first- and second-order moments of the detail coefficients are shown in Figures 4(b) and (c), respectively. The first-order moment M_1 shows some deviations from zero, and the absolute values are smaller than 6% of the standard deviation of the signal for both the Gaussian noise and spectral signal cases. These are stochastic errors of the given signals, and they are expected to decrease by taking the ensemble average. The second-order moment for the Gaussian noise shows the scaling close to d_V^{-2}, and that for the spectral signal shows a peak around $d_V \approx 10^{-1}$. These characteristics of the second-order moments can be discussed based on the wavelet energy spectrum defined below. Here, we define the volume-based wave number as $k_V = \pi/d_V$, because the wavelength for each wavelet is given by the pair of neighboring volumes. The wavelet energy spectrum is then defined as

$$E_{\mathrm{MR}}(k_V) = \frac{N^l M_2[\sigma_i^l d_i^l]}{(2\pi)^D \Delta k_V}, \tag{4.2}$$

where Δk_V is the bandwidth of the wavelets at each level l and is approximately determined as $\Delta k_V = (2^{1/D} - 1)k_V \ln 2/D$. Note that the wavelet energy spectrum is defined based on the coefficient in the L^2 normalization by multiplying with the scaling factor σ_i^l so that the spectrum has the same scaling as the Fourier spectrum. Figure 4(d) shows the wavelet energy spectrum. $E_{\mathrm{MR}}(k_V)$ for the Gaussian noise is approximately proportional to k_V, as expected for the Fourier energy spectrum. $E_{\mathrm{MR}}(k_V)$ for the spectral

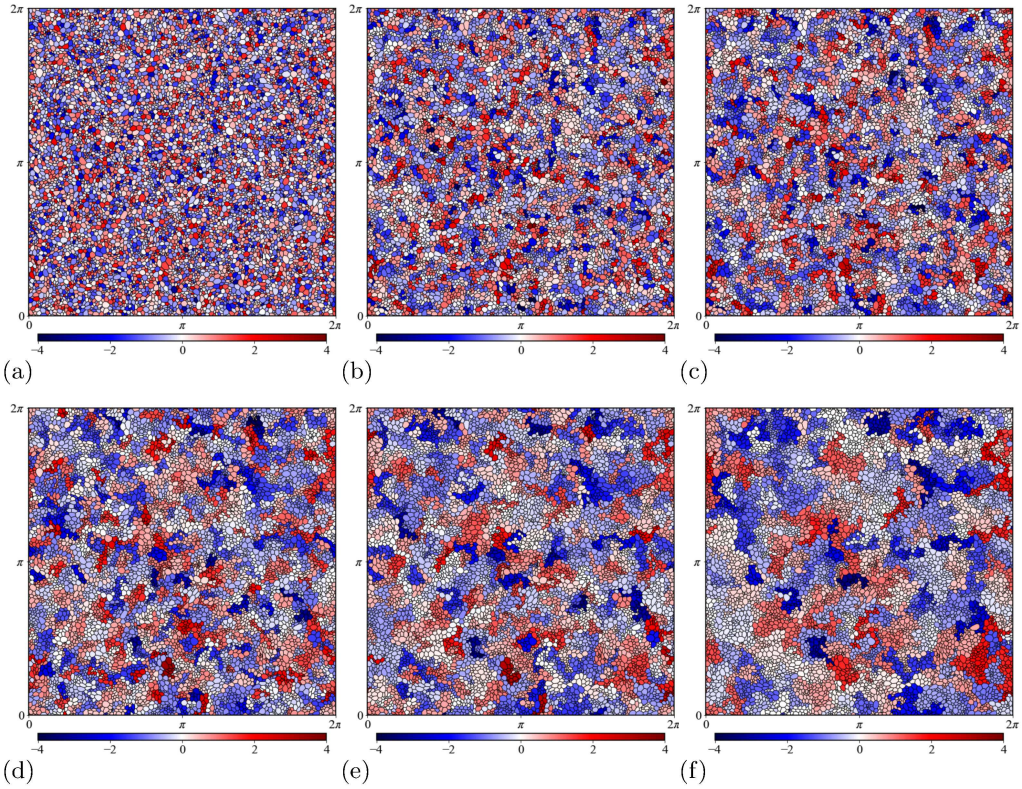

FIGURE 3. Multiresolution tessellation for a 2D uniform random particle distribution for levels (a) 0, (b) 1, (c) 2, (d) 3, (e) 4, and (f) 5. The number of particles is $N_p = 10^4$. The tessellation cells are colored with the coarse-grained signals based on the Gaussian random noise.

signal shows rapid decay for $k_V \gtrsim k_c$, having a peak around $k \sim k_c$. These results are consistent with the characteristics of the Fourier energy spectra for these signals. Therefore, we can conclude that the present multiresolution technique can capture the scale dependence of the signals at particle positions.

5. Application to 3D isotropic turbulence

We apply the proposed multiresolution technique to the particle velocity divergence $\mathcal{D}$ for inertial particles in 3D HIT, i.e., $s_i^0 = \mathcal{D}(\boldsymbol{x}_{p,i})$. We used the particle position and velocity data obtained from the DNS by Matsuda *et al.* (2014). The HIT was computed in the cubic computational domain with edge length 2π. The number of grid points is 512^3, and the Taylor microscale Reynolds number is $Re_\lambda = 204$. The Stokes number based on the Kolmogorov time τ_η (i.e., $St \equiv \tau_p/\tau_\eta$) is $St = 1.0$. The number of particles is $N_p = 1.5 \times 10^7$. The mean particle number density is $\langle n \rangle \eta^3 = 0.030$. The particle velocity divergence $\mathcal{D}$ is calculated by the tessellation technique described in Section 2.

Figure 5(a) shows the PDF of volume V_i^l for each level l for inertial particles in HIT. Similar to the 2D random particles, the peak of the PDF moves to larger volumes as the level increases. However, the separation of the scale is not as clear as in the 2D case because the variance of the tessellation cell volume for clustering particles is larger than that for random particles. Figure 5(b) shows the PDF of projected values of $\mathcal{D}$ for

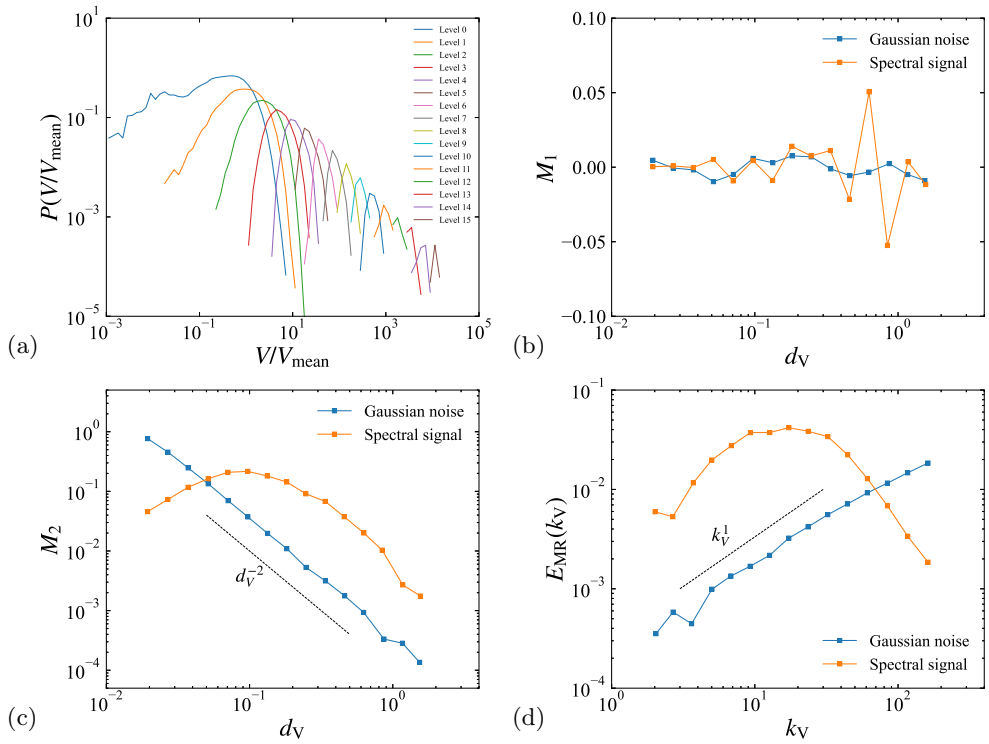

FIGURE 4. (a) Probability density functions (PDFs) of volume, (b) first and (c) second order moments of detail coefficients, and (d) wavelet spectra for the Gaussian noise and the spectral signal at random particles for $N_p = 10^5$.

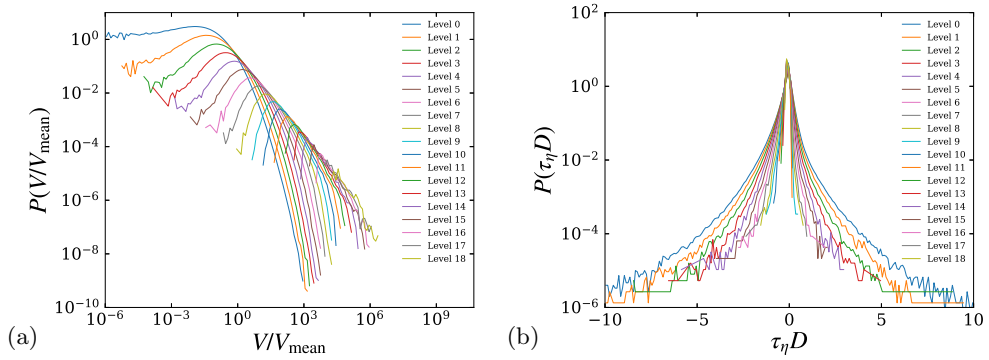

FIGURE 5. Probability density functions (PDFs) of (a) volume and (b) projected particle velocity divergence for inertial particles in HIT for $Re_\lambda = 204$, $St = 1$, and $N_p = 1.5 \times 10^7$.

each level l. The PDF becomes narrower as the level increases. This confirms that the present multiresolution technique can be used for coarse-graining the divergence values at discrete particle positions.

Figure 6(a) shows the wavelet energy spectrum. The scaling of $E_{\mathrm{MR}}(k_V)$ changes around $k_V\eta \approx 0.2$. This scale is close to the peak wave number of the Fourier energy spectrum of the number density ($k\eta \approx 0.2$) reported by Matsuda *et al.* (2014). To compare $E_{\mathrm{MR}}(k_V)$ with the Fourier spectrum, we computed the Fourier spectrum of $n(\boldsymbol{x})\mathcal{D}(\boldsymbol{x})$,

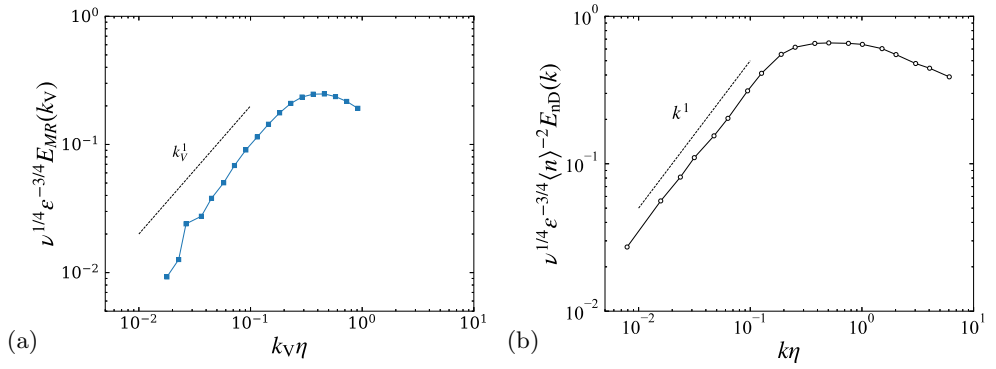

FIGURE 6. (a) Wavelet energy spectrum and (b) Fourier energy spectrum of the particle velocity divergence $\mathcal{D}$ for inertial particles in HIT for $Re_\lambda = 204$, $St = 1.0$, and $N_p = 1.5 \times 10^7$.

i.e., $E_{nD}(k) = \sum_{k-1/2\le|\boldsymbol{k}|<k+1/2} \widehat{n\mathcal{D}}(\boldsymbol{k})\widehat{n\mathcal{D}}^*(\boldsymbol{k})$, where $\widehat{n\mathcal{D}}(\boldsymbol{k})$ is the Fourier coefficient of $n(\boldsymbol{x})\mathcal{D}(\boldsymbol{x})$ and is computed by the analytical Fourier transform (Matsuda *et al.* 2014): Since the divergence values are defined only at particle positions, the spatial distribution of $n(\boldsymbol{x})\mathcal{D}(\boldsymbol{x})$ can be expressed as $n(\boldsymbol{x})\mathcal{D}(\boldsymbol{x}) = \sum_{i=1}^{N_p} \mathcal{D}(\boldsymbol{x}_{p,i})\delta(\boldsymbol{x}-\boldsymbol{x}_{p,i})$, where $\delta(\boldsymbol{x})$ is the Dirac delta function. By applying the Fourier transform, we obtain

$$\widehat{n\mathcal{D}}(\boldsymbol{k}) = (2\pi)^{-3}\sum_{i=1}^{N_p}\mathcal{D}(\boldsymbol{x}_{p,i})\exp(-\iota\boldsymbol{k}\cdot\boldsymbol{x}_{p,i}). \tag{5.1}$$

Note that the divergence data at particle positions inherently contain the information of the particle number density distribution. Thus, the wavelet spectra $E_{\mathrm{MR}}(k_V)$ based on the multiresolution tessellation should be compared with the Fourier spectrum based on Eq. (5.1). Figure 6(b) shows the Fourier spectrum $E_{nD}(k)$. The scaling for $k\eta \lesssim 0.1$ is approximately k^1, and the spectrum values are nearly constant for $0.2 \lesssim k\eta \lesssim 1$. We can confirm that the similar scaling of k_V^1 is observed in the wavelet spectrum $E_{\mathrm{MR}}(k_V)$ for $k_V\eta \gtrsim 0.1$. The peak wave number of $E_{\mathrm{MR}}(k_V)$ is approximately $k_V\eta \approx 0.4$. The narrow wave number range of the peak is due to the broad range of the volume, as shown in Figure 5(a). Therefore, the present multiresolution analysis can appropriately capture the scaling of the multiscale structure of particle velocity divergence of inertial particles in 3D turbulence.

6. Conclusions

We have developed a multiresolution tessellation technique to evaluate multiscale statistics of particle velocity divergence defined at discrete particle positions. The proposed multiresolution technique has been applied to 2D random particle distributions for two test signals, a Gaussian noise and a spectral signal, and a 3D inertial particle distribution with the particle velocity divergence in HIT. We showed that the proposed technique can decompose the signals at different scales depending on the level of multiresolution tessellation, and the validity of the proposed approach has been confirmed by comparing the results with Fourier techniques using a small number of particles. The wavelet approach allows us to decompose coherent and incoherent signals, i.e., denoising, and has been used to extract coherent clusters of inertial particles in turbulent flows (Bassenne *et al.* 2017). Hence, the proposed technique for particle cloud data can be used to extract coherent

structures of particle velocity divergence in particle-laden turbulence without projecting particle cloud data onto Cartesian grids. Moreover, higher-order scale-dependent statistics can be computed, e.g., scale-dependent flatness and skewness (Matsuda *et al.* 2021), based on particle cloud data. These statistics could be important to understanding the multiscale and intermittent behaviors of particles in high–Reynolds number turbulence. Exploring this new multiresolution avenue for particle-laden turbulence is left for future work. In particular, application to the analysis of particle clustering in particle-laden turbulent channel flow is a part of our ongoing investigations (West *et al.* 2022).

REFERENCES

Avena, L., Castell, F., Gaudillière, A. & Mélot, C. 2020 Intertwining wavelets or multiresolution analysis on graphs through random forests. *Appl. Comput. Harmon. A* **48**, 949–992.

Bassenne, M., Urzay, J., Schneider, K. & Moin, P. 2017 Extraction of coherent clusters and grid adaptation in particle-laden turbulence using wavelet filters. *Phys. Rev. Fluids* **2**, 054301.

Cohen, A., Dyn, N., Kaber, S. M. & Postel, M. 2000 Multiresolution schemes on triangles for scalar conservation laws. *J. Comput. Phys.* **161**, 264–286.

Kobbelt, L., Campagna, S., Vorsatz, J. & Seidel, H.-P. 1998 Interactive multiresolution modeling on arbitrary meshes. In *Proceedings of the 25th Annual Conference on Computer Graphics and Interactive Techniques*, pp. 105–114.

Mallat, S. 1999 *A Wavelet Tour of Signal Processing*. Elsevier.

Matsuda, K., Onishi, R., Hirahara, M., Kurose, R., Takahashi, K. & Komori, S. 2014 Influence of microscale turbulent droplet clustering on radar cloud observations. *J. Atmos. Sci.* **71**, 3569–3582.

Matsuda, K., Schneider, K. & Yoshimatsu, K. 2021 Scale-dependent statistics of inertial particle distribution in high Reynolds number turbulence. *Phys. Rev. Fluids* **6**, 064304.

Maxey, M. 1987 The gravitational settling of aerosol particles in homogeneous turbulence and random flow fields. *J. Fluid Mech.* **174**, 441–465.

Oujia, T., Matsuda, K. & Schneider, K. 2020 Divergence and convergence of inertial particles in high-Reynolds-number turbulence. *J. Fluid Mech.* **905**, A14.

Oujia, T., Matsuda, K. & Schneider, K. 2022 Extreme divergence and rotation values of the inertial particle velocity in high Reynolds number turbulence using Delaunay tesselation. In *Proceedings of 12th International Symposium on Turbulence and Shear Flow Phenomena (TSFP12)*.

Shuman, D. I., Narang, S. K., Frossard, P., Ortega, A. & Vandergheynst, P. 2013 The emerging field of signal processing on graphs. *IEEE Signal Proc. Mag.* **30**, 83–98.

West, J., Oujia, T., Matsuda, K., Schneider, K., Jain, S. & Maeda, K. 2022 On divergence and curl of the inertial particle velocity in a four-way coupled channel flow. In *Proceedings of the Summer Program*, Center for Turbulence Research, Stanford University.

Yu, H. J. & Ra, J. B. 1999 Fast triangular mesh approximation of surface data using wavelet coefficients. *Vis. Comput.* **15**, 9–20.